

# Diiridium(III) Complexes with Fluorenylpyridyl Cyclometalating and $\mu_2$ -Oxamidato Bridging Ligands and their High Efficiency Phosphorescent Solution-Processed OLEDs

Ahmed M'hamedi,<sup>[a]</sup> Mark A. Fox,<sup>[b]</sup> Andrei S. Batsanov,<sup>[b]</sup> Hameed A. Al-Attar,<sup>[c]</sup> and Martin R. Bryce<sup>\*[b]</sup>

Three neutral diiridium(III) complexes with 2-fluorenylpyridyl (flpy) or 5-fluoro-2-fluorenylpyridyl (flpyF) as C<sup>^</sup>N cyclometalating ligands and a  $\mu_2$ -oxamidato bridge have been synthesized. NMR spectroscopy shows that the complexes are inseparable mixtures of diastereomers (*rac*,  $\Delta\Delta/\Lambda\Lambda$  and *meso*,  $\Delta\Lambda$ ) with bridges in *anti* and *syn* configurations. Each isomer was determined using <sup>19</sup>F NMR data on the flpyF complex. Single crystal diffraction studies of two complexes revealed *meso* diastereomers with *anti* configuration of the bis-(*t*-butylphenyl)oxamidato bridge but an uncertain configuration of the unsubstituted  $\mu_2$ -oxamidato bridge. The complexes are highly emissive ( $\Phi_{\text{PL}}$  57–82% in solution) with excited state lifetimes of  $\tau_{\text{p}}$  ca. 40  $\mu\text{s}$ . The vibronic emissions with maxima at

553–561 nm and at 587–595 nm in solution are attributed to mixed metal-ligand to ligand charge transfer (<sup>3</sup>MLLCT). Density functional theory (DFT) and time dependent-DFT (TD-DFT) calculations establish the involvement of the fluorenyl groups and the vibronic structures in the emissions. The bridge mediates intramolecular interactions between iridium centers based on electrochemical measurements Phosphorescent organic light-emitting diodes (PhOLEDs) using these complexes as the emissive dopants with a solution-processed active layer have bright greenish-yellow emission with  $\lambda_{\text{max}}^{\text{EL}}$  ca. 560 nm, luminous efficiency up to 26 cd/A and high external quantum efficiency (maximum  $\eta_{\text{ext}}$  ca. 20%).

## Introduction

Cyclometalated iridium(III) complexes possess rich and tuneable photophysical properties by virtue of the extensive variations in their homoleptic and heteroleptic structures. The heavy atom effect promotes efficient spin-orbit coupling (SOC) which converts singlet excited states into triplets and phosphorescence occurs from the lowest triplet state.<sup>[1,2]</sup> The complexes have readily tuneable emission colors by ligand design,<sup>[2]</sup> and

they typically possess phosphorescent lifetimes on the micro-second timescale, high quantum efficiencies and good stability, which has favored their widespread optoelectronic applications. They are most famously used as emitters in phosphorescent organic light emitting devices (PhOLEDs).<sup>[3–5]</sup> Their excellent emissive properties have also led to applications in light-emitting electrochemical cells,<sup>[6,7]</sup> in biolabeling and biosensing,<sup>[8]</sup> as photosensitisers for theranostics,<sup>[9]</sup> as materials for photocatalytic hydrogen evolution<sup>[10]</sup> and for nanophotonic information processing and storage.<sup>[11]</sup>

Most of these complexes are monoiridium species; however, diiridium complexes are now gaining increased attention. The presence of an additional metal center can augment SOC pathways, and the bridging ligand can impart new and interesting structural, electronic and photophysical properties compared to monoiridium analogs.<sup>[12,13]</sup> Representative bridging ligands in diiridium complexes include pyrimidine,<sup>[14,15]</sup> 2-phenylpyrimidine,<sup>[16,17]</sup> diarylhydrazide,<sup>[18,19]</sup> pyrazolate,<sup>[20,21]</sup> bis(phenanthroline)<sup>[22]</sup> Schiff bases,<sup>[22–25]</sup> pyridazine,<sup>[26]</sup> butadiene,<sup>[27]</sup> alkynes<sup>[28]</sup> and phenyltetrazole.<sup>[29]</sup> The presence of two chiral octahedral Ir(III) metal centers in the same molecule means that the dinuclear complexes are formed as a mixture of diastereomers which are usually not separated. An important strategy to obtain high photoluminescence quantum yield (PLQY) is to expand the aromatic system of ligands and utilize rigid ligands to confine non-radiative exciton decays.<sup>[30]</sup>

Sünkel *et al* first reported a neutral diiridium complex bridged by a  $\mu_2$ -oxamidato-*N,N',O,O'* ligand, namely  $[\text{Ir}_2(\mu_2\text{-oxamidato})(\text{ptpy})_4]$  [ $\text{ptpy} = 2\text{-}(p\text{-tolyl})\text{pyridinato}$ ].<sup>[31]</sup> Subse-

[a] Dr. A. M'hamedi  
Department of Chemistry, College of Sciences and Humanities in Al-Kharj,  
Prince Sattam bin Abdulaziz University, Al Kharj 11942, Saudi Arabia  
and  
Department of Chemistry, University of Abdelhamid Ibn Badis BP 227,  
Mostaganem 27000, Algeria

[b] Dr. M. A. Fox, Dr. A. S. Batsanov, Prof. M. R. Bryce  
Department of Chemistry, Durham University, South Road, Durham, DH1  
3LE, UK  
E-mail: m.r.bryce@durham.ac.uk  
Homepage: <https://www.durham.ac.uk/staff/m-r-bryce/>

[c] Dr. H. A. Al-Attar  
Department of Physics, College of Science, University of Basrah, Basrah, Iraq  
and  
Department of Physics, Durham University, South Road, Durham, DH1 3LE,  
UK

Supporting information for this article is available on the WWW under  
<https://doi.org/10.1002/ejic.202400745>

© 2024 The Author(s). European Journal of Inorganic Chemistry published by  
Wiley-VCH GmbH. This is an open access article under the terms of the  
Creative Commons Attribution License, which permits use, distribution and  
reproduction in any medium, provided the original work is properly cited.

quently we characterized analogs with 4-mesityl-6-phenylpyridyl cyclometalating ligands.<sup>[32,33]</sup> These complexes are all green emitters with  $\lambda_{\text{max}}^{\text{PL}}$  ca. 520 nm and PLQYs 60–70% in solution.<sup>[31–33]</sup> PhOLEDs with the complexes as dopants in a solution-processed emitting layer had  $\lambda_{\text{max}}^{\text{EL}}$  533 nm and low maximum external quantum efficiency (EQE)  $\eta_{\text{ext}}$  ca. 3–3.5% and luminous efficiency  $\eta_{\text{L}}^{\text{max}}$  13 cd/A.<sup>[32]</sup> More recent analogs with 2-methyl-6-phenylpyridyl cyclometalating ligands and a  $\mu_2$ -oxamidato-*N,N',O,O'* bridge surprisingly had very low PLQYs (ca. 1%); therefore, these complexes are not suitable for device applications.<sup>[34]</sup>

We have now extended the range of diiridium complexes bridged by a  $\mu_2$ -oxamidato-*N,N',O,O'* ligand by exploiting 2-fluorenylpyridyl (flpy) and 5-fluoro-2-fluorenylpyridyl (flpyF) cyclometalating ligands. Most significantly, the new complexes 1–3 (Figure 1) are strongly emissive in solution and their PhOLEDs with a solution-processed emissive layer have greenish-yellow emission with  $\lambda_{\text{max}}^{\text{EL}}$  ca. 560 nm, luminous efficiency up to 26 cd/A and high external quantum efficiency ( $\eta_{\text{ext}}^{\text{max}}$  ca. 20%). The performance of these devices vastly exceeds the previous  $\mu_2$ -oxamidato-*N,N',O,O'* bridged analogs discussed above<sup>[32]</sup> and is competitive with the best diiridium-based PhOLEDs reported to date.

## Results and Discussion

### Synthesis and Characterization

Fluorenylpyridine (flpyH) ligands were chosen for the present study because they have previously been used in Ir complexes that are thermally stable, highly luminescent and solution processable for PhOLED fabrication<sup>[35–37]</sup> Hexyl chains were attached to the fluorene units to give the complexes good solubility in a range of organic solvents. The synthesis of complexes 1–3 proceeded by reactions of the  $\mu_2$ -dichloro-bridged precursor  $[\text{Ir}(\text{flpy})_2\text{Cl}_2]$ <sup>[37]</sup> or  $[\text{Ir}(\text{flpyF})_2\text{Cl}_2]$ <sup>[37]</sup> with oxamide or with *N,N'*-di(*t*-butyl)phenyloxalamide in the presence of sodium methoxide, following previous procedures.<sup>[34]</sup> The molecular formulae of the complexes were established unambiguously by elemental analysis and mass spectrometry. The thermal stabilities of the complexes were assessed by differ-

ential scanning calorimetry (DSC) and thermal gravimetric analysis (TGA) (Figures S19–S20). The 5% weight loss temperatures ( $T_{5\%}$ ) are  $> 300^\circ\text{C}$  for all the complexes, suggesting that they should be thermally stable under PhOLED operating conditions.

It is known that bimetallic complexes bridged with  $\mu_2$ -oxamidato-*N,N',O,O'* and related ligands form as a mixture of diastereomers.<sup>[38]</sup> In previous  $\mu_2$ -oxamidato-*N,N',O,O'* bridged diiridium complexes with different C^N ligands,<sup>[31,32,34]</sup> diastereomeric mixtures comprising enantiomers with the same ( $\Delta\Delta$  or  $\Lambda\Lambda$ ) configurations of the two octahedral Ir centers (*rac*), and the *meso* ( $\Delta\Lambda$ ) form along with the possible *syn* and *anti* bridge forms – four isomers in all – were reported. Remarkably, one isomer was found to be the major product ( $> 75\%$ ) in  $\mu_2$ -oxamidato-*N,N',O,O'* bridged diiridium complexes 1 and 3 based on their NMR spectra here. These findings suggest that the fluorenylpyridyl (flpy) C^N ligand – unlike other C^N ligands reported<sup>[31,32,34]</sup> previously – plays an important role in favoring one isomer of the  $\mu_2$ -oxamidato-*N,N',O,O'* bridged diiridium complex over the other three isomers. Unfortunately, proton ( $^1\text{H}$ ) and carbon-13 ( $^{13}\text{C}\{^1\text{H}\}$ ) NMR data for 1 and 3 do not identify the preferred isomer as all four isomers have the same expected number of peaks and patterns.

In contrast with the one major isomer found in flpy complexes 1 and 3, complex 2 with the fluorine-substituted fluorenylpyridyl (flpyF) C^N ligand gave a complicated set of peaks in the  $^1\text{H}$  and  $^{13}\text{C}\{^1\text{H}\}$  NMR spectra indicating a mixture of each isomer present in non-equivalent amounts. Each isomer could be assigned by NMR for  $\mu_2$ -oxamidato-*N,N',O,O'* bridged diiridium complexes for the first time here with complex 2 due to the fluorine substituent and the use of  $^{19}\text{F}$  NMR. The  $^{19}\text{F}\{^1\text{H}\}$  NMR spectrum of 2 consists of four isomers labelled A:B:C:D in a 40:1:20:39 peak intensity ratio in Figure 2. Each isomer has two non-equivalent sets of fluorine atoms  $\text{F}^1$  and  $\text{F}^2$  as shown in Figure 3; thus two  $^{19}\text{F}$  peaks of equivalent intensities per isomer are expected. Both isomers A and B contain doublets with  $J_{\text{FF}}$  coupling constants of 23 Hz whereas C contains singlets and D has doublets with  $J_{\text{FF}}$  coupling constants of 7 Hz. Based on the assumption that the nearest  $\text{F}^1\dots\text{F}^2$  distances are inversely proportional to the magnitude of the  $J_{\text{FF}}$  coupling constant, C is assigned to the *anti rac* isomer and D to the *syn rac* isomer (Table 1). It is remarkable that the *syn* configuration is preferred

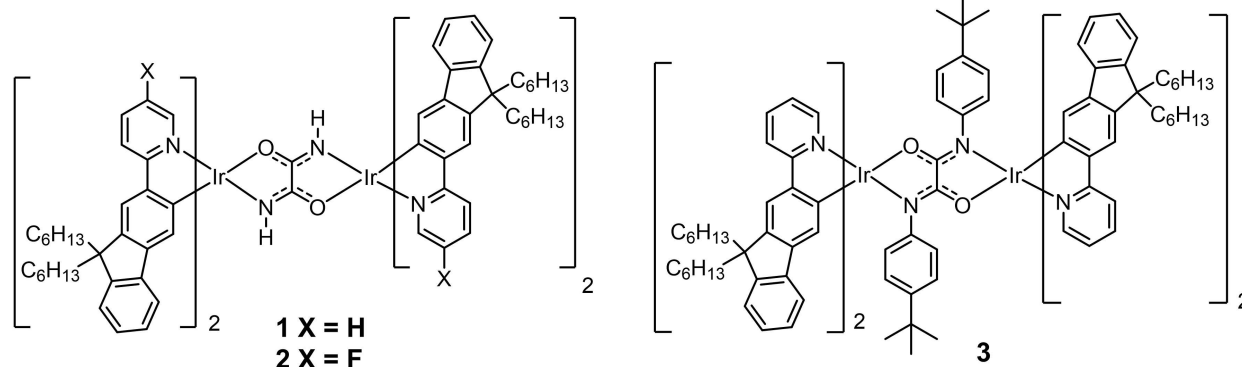


Figure 1. Structures of the  $\mu_2$ -oxamidato-*N,N',O,O'* bridged diiridium complexes 1–3 synthesized in this study.

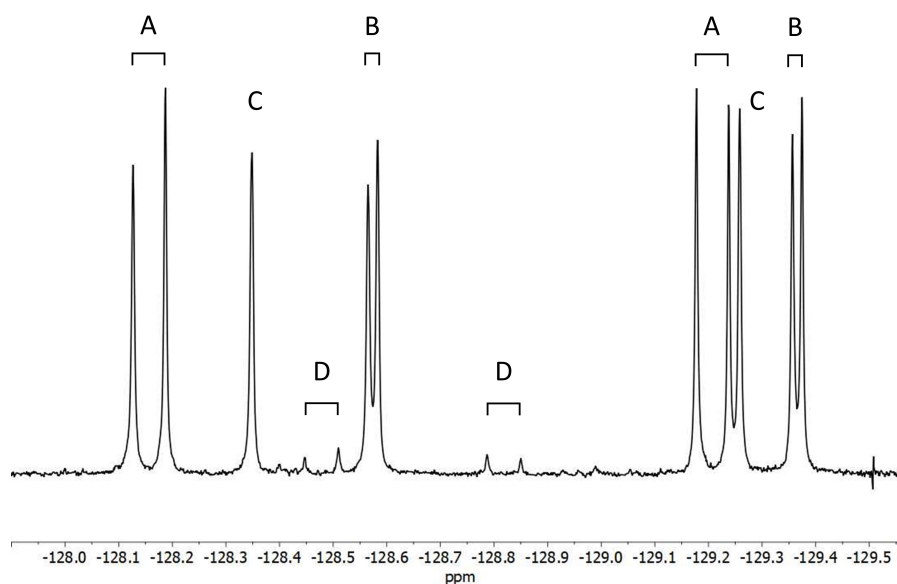


Figure 2. 374 MHz  $^{19}\text{F}\{^1\text{H}\}$  NMR spectrum of **2** in  $\text{CDCl}_3$ .

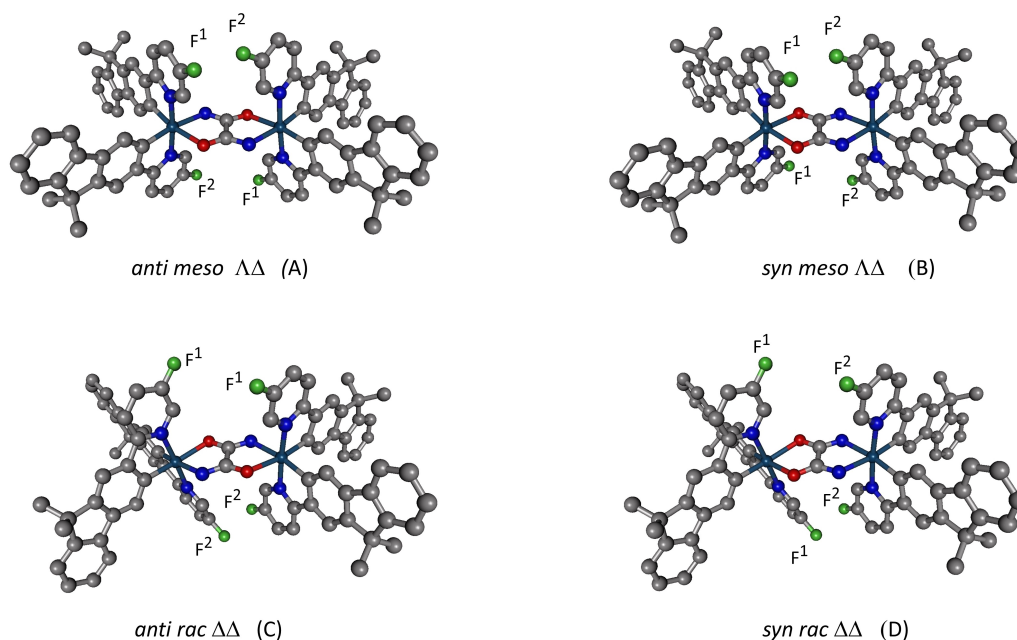


Figure 3. The four isomers of **2** with hydrogens and  $\text{C}_5\text{H}_{11}$  groups removed for clarity.

Isomer	$^{19}\text{F}$ NMR (ppm)	$J_{\text{FF}}$ coupling constant (Hz)	$\text{F}^1\dots\text{F}^2$ distance (Å)	Relative peak intensity	Assigned isomer peaks
A	-128.2, -129.2	23	3.21	40	<i>anti meso</i>
B	-128.5, -128.8	23	3.33	1	<i>syn meso</i>
C	-128.3, -129.3	-	10.40	20	<i>anti rac</i>
D	-128.6, -129.4	7	3.74	39	<i>syn rac</i>

over *anti* here for the *rac* forms of **2**. The identities of A and B are not straightforward with similar  $\text{F}^1\dots\text{F}^2$

coupling constants, but the crystal structure study (*vide infra*) on the major isomer of **1** revealed the *anti* configuration. Isomer

A is therefore tentatively assigned as *anti meso* and the minor isomer B as the *syn meso* form.

### Crystal Structures

The X-ray diffraction analysis of **1** and **3** was performed on single crystals grown from mixtures of isomers in solution. Both crystallized in centrosymmetric space groups,  $P\bar{1}$  (**1**) and  $P2_1/c$  (**3**); the molecule lies at a crystallographic inversion center and thus has *meso* ( $\Delta\Lambda$ ) configuration of the metal centers. Each Ir atom has a distorted octahedral coordination (Table 2) with two fluorenylpyridyl ( $C^{\wedge}N$ ) ligands having their N atoms *trans* to one another and their C atoms *trans* to the O or N atoms of the bridging ligand, as observed previously for  $\mu_2$ -oxamidato- $N,N',O,O'$  bridged diiridium with different ( $C^{\wedge}N$ ) ligands.<sup>[31–34]</sup> However, in both cases the picture is complicated by disorder. In structure **1** (Figure 4), the NH and O of the oxamidato bridge are statistically mixed in both independent positions ( $\underline{A}$  and  $\underline{B}$ ) in practically equal ratios, hence the crystallographic  $C_i$  symmetry does not conclusively prove the *anti*-configuration of the bridge. In each position, the O and N atoms could not be resolved and were refined as a single atom with mixed scattering factor. Furthermore, the residual electron density map reveals a strong peak at *ca.* 1 Å from the Ir atom, which can be refined as a minor [with 0.068(4) occupancy] position of the latter, suggesting the presence of more extensive disorder, which was unambiguously observed in the structure of **3** (*vide infra*), although the positions of lighter atoms in **1** could not be revealed. The structure of **1** contains continuous channels parallel to the *a* axis and filled with randomly disordered solvent, presumably three molecules of pentane per molecule of **1** (see Experimental).

In structure **3** (Figure 5) the entire molecule is disordered in a 0.74:0.26 ratio between two orientations,  $\underline{A}$  and  $\underline{B}$ , both of which are genuinely centrosymmetric and have *anti* configurations of the oxamidato bridge, but with O and N atoms in opposite positions (Figure 5). In this case, all alternative positions of the bridge atoms were resolved and refined separately. In component  $\underline{A}$ , the *t*-butyl-phenyl substituent is disordered between two orientations (the planes of the arene

**Table 2.** Selected bond distances (Å) in structures *meso* **1** and *anti meso* **3**.

	1, $\underline{A}$	1, $\underline{B}$	3, $\underline{A}$	3, $\underline{B}$
Ir–O(1)	2.146(9)	2.149(8)	2.131(9)	2.07(5)
Ir–N(1)	2.149(8)	2.146(9)	2.181(13)	2.16(3)
Ir–N(2)	2.031(10)		2.021(12)	1.93(3)
Ir–N(3)	2.023(11)		2.014(11)	1.97(2)
Ir–C(1)	2.018(15)		1.979(13)	1.94(3)
Ir–C(19)	2.007(11)		1.970(13)	2.02(3)
C(0)–O(1)	1.296(13)	1.274(14)	1.311(12)	1.28(3)
C(0')–N(1)	1.274(14)	1.296(13)	1.264(13)	1.28(3)
C(0)–C(0')	1.53(2)		1.501(18)	1.55(10)
Ir...Ir	5.669		5.666	5.684

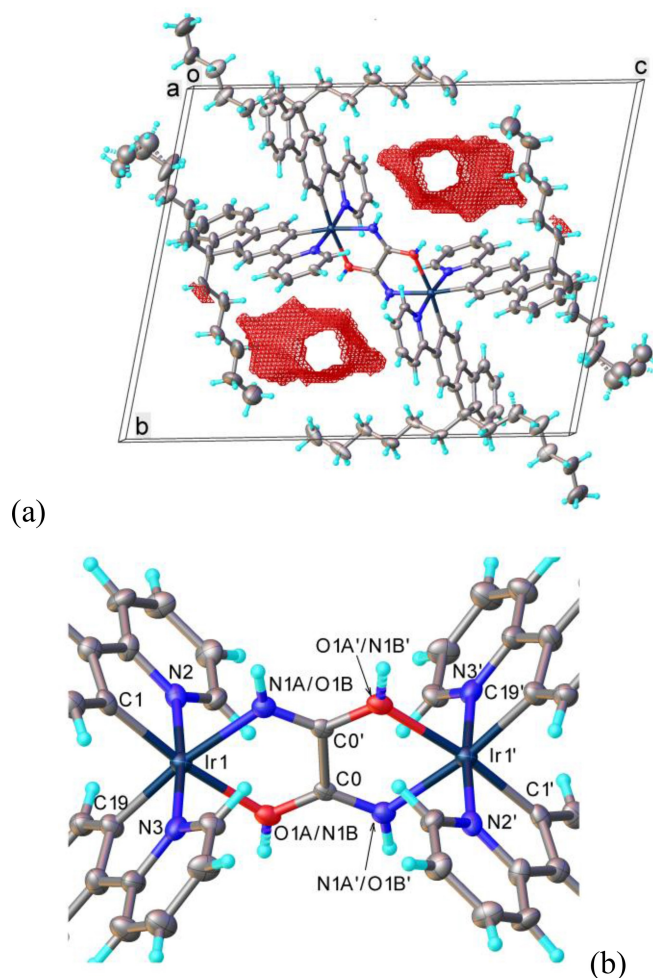


**Figure 4.** (a) X-ray crystal structure of *meso* **1**. Atomic displacement ellipsoids are drawn at 30% probability level, red contours show solvent-containing channels. (b) Metal coordination. Atoms generated by the inversion center are primed.

rings forming a dihedral angle of 47°) with the methyl C(44) atom coinciding, while in the same substituent of component  $\underline{B}$  the *t*-butyl group shows a random rotational disorder (modelled by two opposite orientations). The *n*-hexyl chains show further disorder and generally very large atomic displacement parameters. Although the crystal packing is rather loose, the structure contains no solvent of crystallization and no solvent-accessible voids.

### Electrochemistry

The redox properties of the new complexes **1–3** were studied by cyclic voltammetry (CV) (Figure 6 and Table 3). They display two quasi-reversible, one-electron oxidation waves assigned to stepwise oxidation of the metal centered  $Ir^{3+}/Ir^{4+}$  redox couples. The two oxidation potentials ( $E_2^{Ox1}$  and  $E_2^{Ox2}$ ) and potential differences ( $\Delta E_2$ ) for **1** and **3** are essentially identical reflecting little effect of the different bridges on the oxidations; thus the bridges do not appear to be involved in the HOMOs.

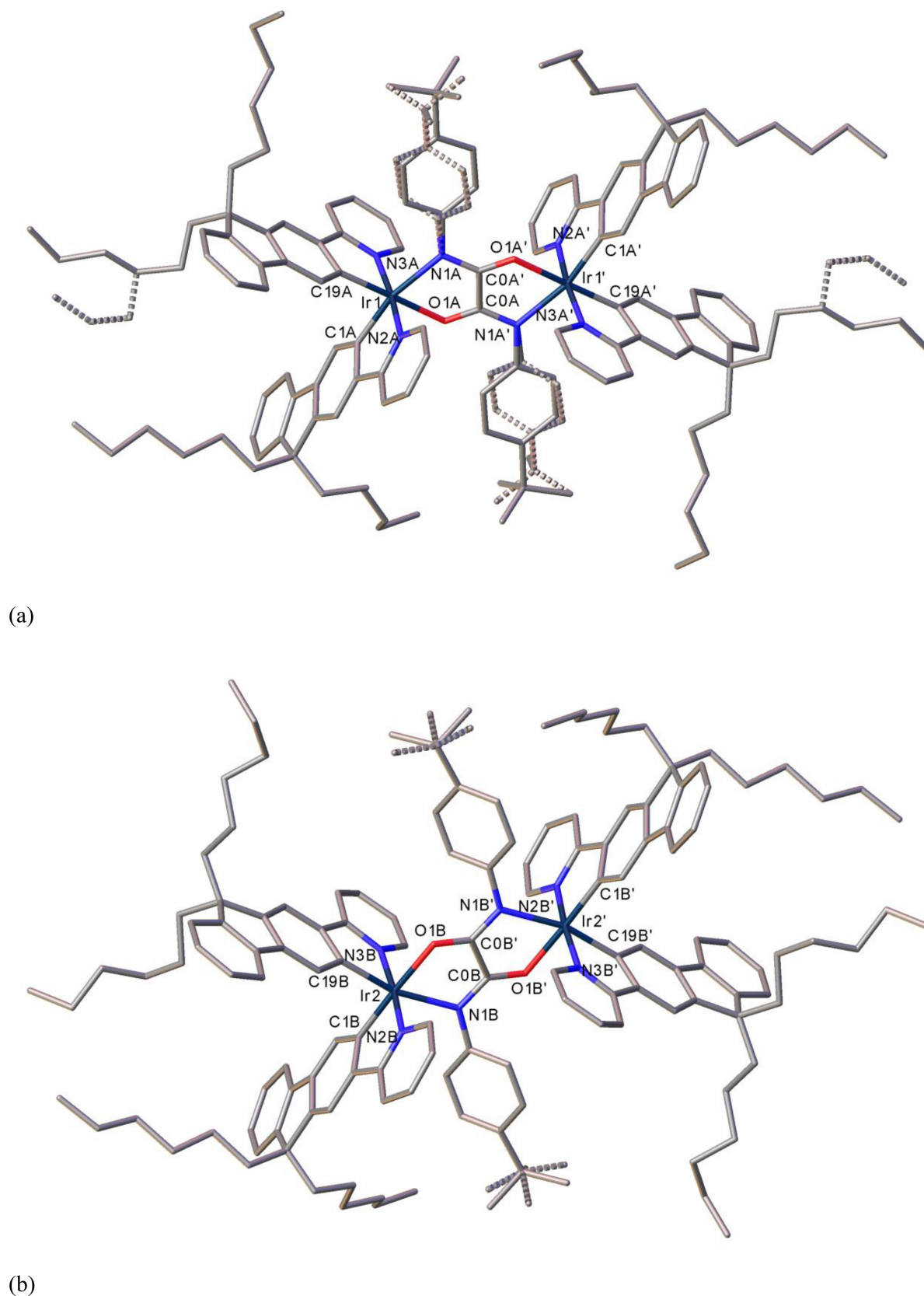


**Figure 5.** The major (a, 74%) and minor (b, 26%) components sharing the same crystallographic site in the structure of *anti meso* 3, shown in the same aspect. Atoms generated by the inversion center are primed; H atoms are omitted for clarity. Stippled fragments indicate further disorder.

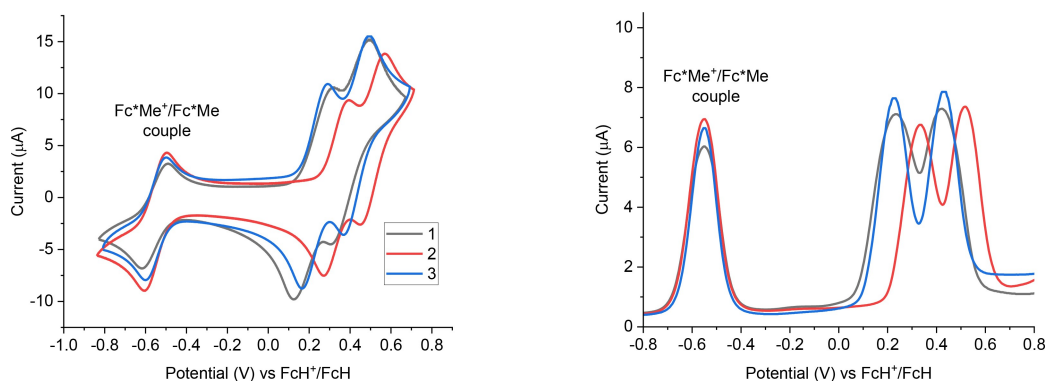


Figure 6. Cyclic (left) and square wave (right) voltammetry traces for complexes 1–3.

Complex	$E_2^{Ox1}$ (V) <sup>a</sup>	$E_2^{Ox2}$ (V) <sup>[a]</sup>	$\Delta E_2$ (mV) <sup>[a]</sup>	Ir...Ir (Å)	HOMO (eV) <sup>[b]</sup>	HOMO (eV) <sup>[c]</sup>
1	0.23	0.42	190	5.778	−5.03	−4.79
2	0.33	0.52	190	5.764	−5.14	−4.93
3	0.23	0.43	200	5.792	−5.03	−4.81

[a] 0.1 M (<sup>n</sup>Bu<sub>4</sub>NPF<sub>6</sub>) in deaerated DCM solutions at 298 K, scan rate 100 mV s<sup>−1</sup>, referenced to the internal decamethylferrocene/decamethylferrocenium couple (Fc\*Me/Fc\*Me<sup>+</sup>) at −0.55 V with the ferrocenium/ferrocene (FcH/FcH<sup>+</sup>) couple as reference at 0.00 V. [b] HOMO levels calculated from CV potentials by HOMO = −4.8 + (−E<sub>2</sub><sup>Ox1</sup>), using ferrocene as the standard. [c] HOMO energies calculated from optimized geometries of model geometries of *anti meso* isomers 1–3 at B3LYP/LANL2DZ:3-21G\*.

These observations differ from complexes with 4-mesityl-6-phenylpyridyl as C<sup>^</sup>N ligands where the bridges are involved in the HOMOs.<sup>[32]</sup> Higher oxidation potentials by +0.1 V with a similar potential difference  $\Delta E_2$  were found for 2 compared to 1 and 3. The oxidation potential changes are merely due to the electron-withdrawing fluorine at each fplyF ligand in 2. All observed oxidation potentials suggest that the fluorenyl C<sup>^</sup>N ligands are involved in the HOMOs of 1–3. The similar  $\Delta E_2$  values for all complexes reflect the same intramolecular interaction present after the first oxidation at one iridium center resulting in a more difficult oxidation of the second iridium center in each complex.

### Photophysics

The photophysical data for complexes 1–3 are listed in Table 4. The absorption spectral profiles of all three complexes in 2-

methyltetrahydrofuran (2-MeTHF) solutions are very similar (Figure 7). The high energy bands are attributed to characteristic ligand-centered (LC) spin-allowed  $\pi$ - $\pi^*$  transitions. Extending towards longer wavelengths, the complexes reveal a sequence of comparatively weaker peaks, ranging between 375 and 550 nm. These are assigned to singlet and triplet mixed metal-ligand to ligand charge transfer states (<sup>1</sup>MLLCT and <sup>3</sup>MLLCT). The lower energy MLLCT bands, ranging from 480 to 550 nm, are designated as the spin-forbidden triplet <sup>3</sup>MLLCT absorptions.<sup>[39,40]</sup> The molar extinction coefficients are consistent with literature data for analogous diiridium complexes.<sup>[31,34,37]</sup>

All three complexes are intensely photoluminescent in solution at room temperature. The PL spectra (Figure 8) are very similar, featuring distinct peaks at  $\lambda_{max}$  561 nm for 1 and 2 and 553 nm for 3, along with discernible lower-energy shoulder peaks clearly observed at room temperature which reflect the high rigidity of the complexes. The emission peaks are notably red-shifted by ca. 40 nm compared to previous analogs with

Complex	$\lambda_{max}^{Abs}$ / nm <sup>[a]</sup>	$\lambda_{max}^{PL}$ / nm <sup>[b]</sup>	$\tau_p$ / $\mu$ s <sup>[c]</sup>	PLQY <sup>[d]</sup> / $\Phi_{PL}$ %	Rad. rate $k_r$ <sup>[e]</sup> (s <sup>−1</sup> )
1	320, 340, 405, 447, 490	561, 595	47	72	$1.53 \times 10^4$
2	316, 340, 405, 440, 480	561, 595	44.7	82	$1.83 \times 10^4$
3	330, 340, 405, 443, 483	553, 587	42.66	57	$1.34 \times 10^4$

[a] Data obtained in 10  $\mu$ M 2-MeTHF solutions at 20 °C. [b] Data obtained in degassed 2-MeTHF solution with excitation wavelength 360 nm. [c] The phosphorescence decay lifetimes of thin films prepared by spin-coating on quartz substrate from chlorobenzene solutions in poly(methyl methacrylate) (PMMA): estimated error  $\pm$  5%. [d] Measured relative to 9,10-diphenylanthracene: estimated error  $\pm$  5%. [e]  $k_r = \Phi_{PL} / \tau_p$ .

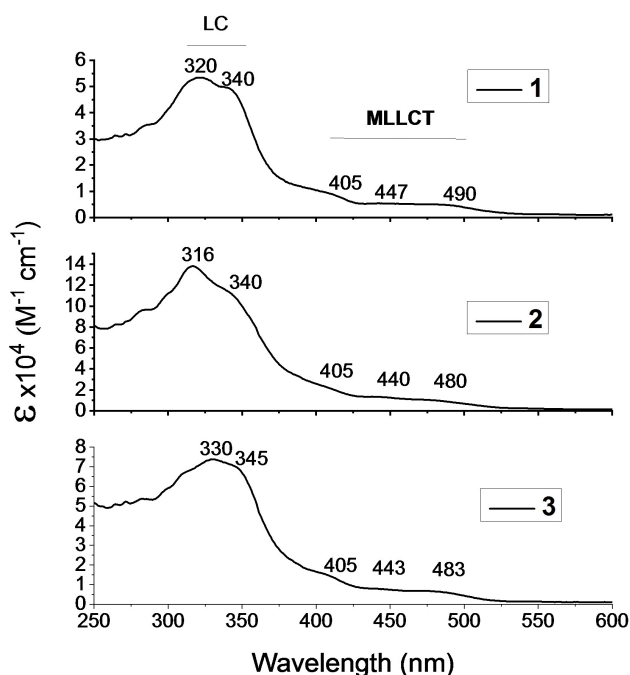


Figure 7. Absorption spectra of complexes 1, 2 and 3 in 2-MeTHF (concentration = 10  $\mu$ M) at 20  $^{\circ}$ C.

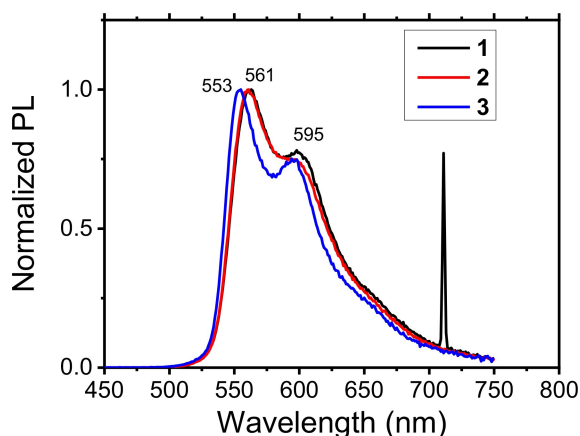


Figure 8. Photoluminescence spectra of complexes 1–3 in 2-methylTHF at 20  $^{\circ}$ C; excitation wavelength 360 nm.

phenylpyridine ligands.<sup>[31–33]</sup> due to the  $\pi$ -extension in the fluorenylpyridine ligands.<sup>[35,36]</sup>

The phosphorescence decay lifetimes of thin films of the complexes 1, 2 and 3 prepared by spin-coating on quartz substrate from chlorobenzene solutions in poly(methyl methacrylate) (PMMA) are shown in Figure 9. All the complexes show relatively long lifetimes ranging from 43 to 47  $\mu$ s, originating from  $^3$ MLLCT transitions, indicating strong spin-orbital coupling with the singlet states.

## Computations

Optimized model geometries of 1–3 with methyl groups in place of hexyl groups at B3LYP/LANL2DZ:3-21G\* showed negligible energy differences between the four isomers with the largest energy difference of 2.6 kcal mol $^{-1}$  found between *anti meso* and *anti rac* isomers in 2 (Table S3). These values indicate that the preferred *anti meso* isomers found experimentally for 1 and 3 are formed kinetically, not thermodynamically, with lower transition state (TS) energies to *anti meso* isomers in the reaction pathways compared to TS energies in the reaction pathways to other isomers. The lack of a dominant diiridium complex isomer in 2 suggests that the flypF ligands do not significantly influence the TS reaction energies to generate a major isomer product. Electronic structure calculations on model *anti meso* isomers of 1–3 showed the trend between observed oxidation potentials and computed HOMO energies to be in excellent agreement with 2 computed to be at ca 0.1 eV lower in HOMO energy compared to those for 1 and 3 (Table 3). The HOMOs are on the iridium and fluorenyl units in 1–3 in agreement with experimental oxidation potentials whereas the LUMOs are mainly at the pyridyl moieties (Figure S21). There are no significant bridge contributions to the frontier orbitals in agreement with the observed consistent  $\Delta E_{\frac{1}{2}}^{\text{Ox1}}$  values and Ir...Ir distances for 1–3 (Table 3).

Time-dependent DFT (TD-DFT) calculations on  $S_0$  model geometries confirm the assigned LC and MLCT transitions in the observed absorption spectra of 1–3 with simulated  $S_0 \rightarrow S_n$  spectra and natural transition orbitals (NTOs) of  $S_0 \rightarrow T_1$  transitions (Figures S22 and S23). The orbital data for the lowest transitions in all three complexes are all similar and are described as iridium-fluorenyl to fluorenyl-pyridyl transitions from their NTO contribution percentages. TD-DFT data on  $T_1$  model geometries of 1–3 also reveal similar NTOs for predicted  $S_0 \leftarrow T_1$  emission data (Figure 10) with fluorenyl groups significantly involved in both hole and particle orbitals with 44–57% contributions. Both  $S_0$  and  $T_1$  optimized geometries appear to be similar based on their orbital make-ups and geometry fittings between them confirmed that the geometries remain rigid with fitting errors of only 0.088 – 0.129  $\text{\AA}$  for 1–3 (Figures S24–S26).

Simulated emission spectra of 1–3 were generated from both  $S_0$  and  $T_1$  optimized model geometries via the adiabatic Hessians (AH) method (Figure 11). The emission shapes and the emission maxima are in very good agreement with the observed emission spectra (Figure 8). The vibronic structures in the emissions arise from the rigidity of the geometries combined with the substantial orbital contributions of the fluorenyl groups.

## Electrophosphorescent OLED Characterization

All the complexes readily dissolved in chlorobenzene without any aggregated particulates and devices were fabricated using a spin-coated single-active emissive layer structure: The final device architecture was: ITO/PEDOT:PSS/PVK–OXD-7(40 wt.%)–

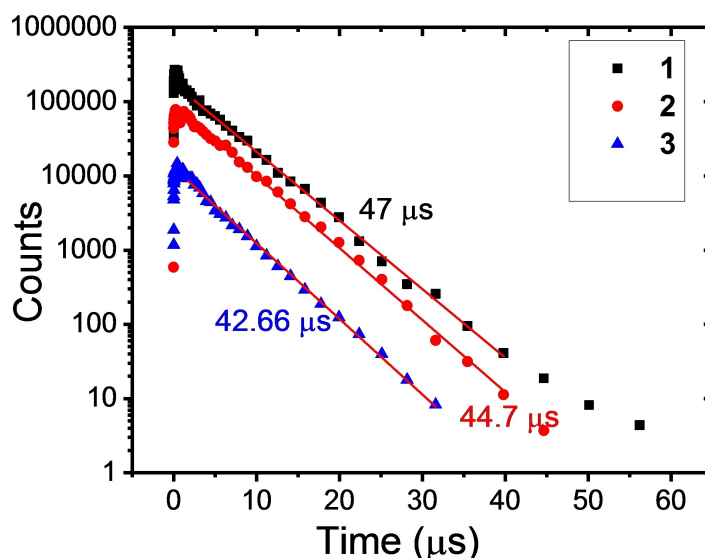


Figure 9. Phosphorescence decays of the complexes doped at 5 wt% in inert PMMA matrix on a log-linear scale; excitation wavelength 355 nm.

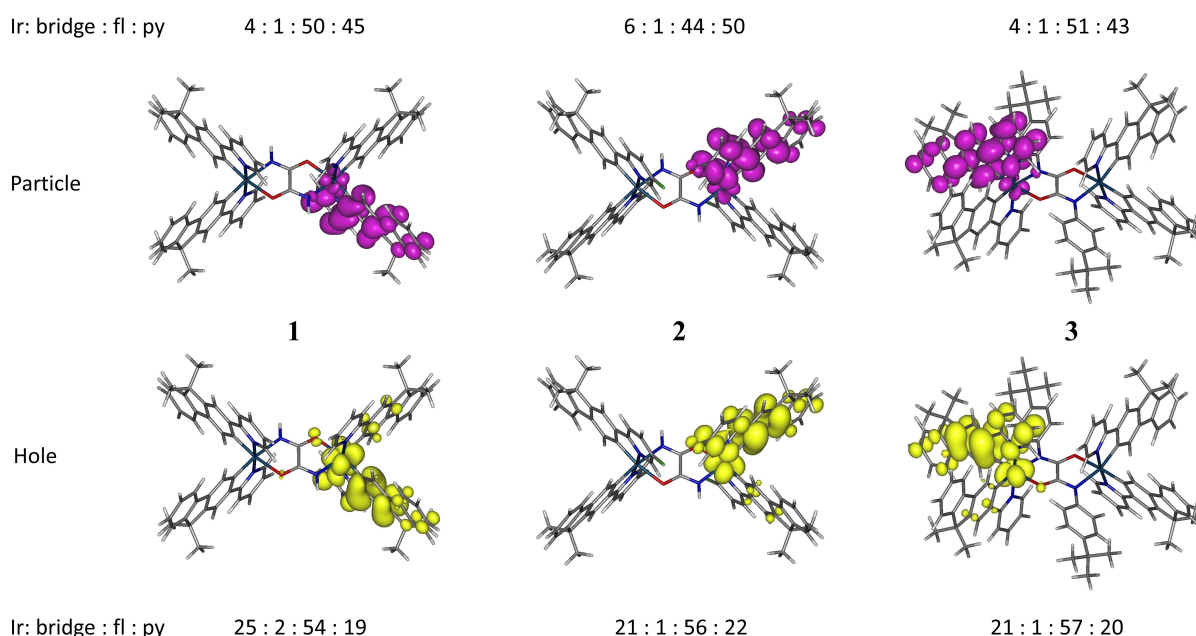
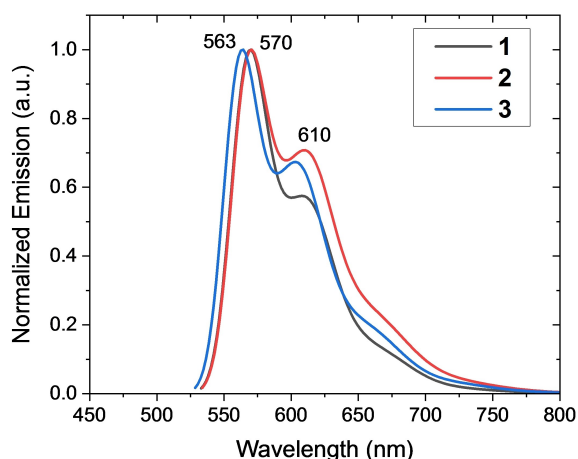


Figure 10. Natural transition orbitals (NTOs) for  $T_1$  model geometries of *anti meso* isomers 1–3.

complex 1, 2 or 3 (2 wt%)/TPBi/BCP/LiF/Al as described in the Experimental section. The electroluminescence (EL) spectra (Figure 12a) have very similar profiles to the PL spectra (Figure 8) demonstrating that the greenish-yellow emission at  $\lambda_{\max}^{\text{EL}}$  ca. 560 nm is exclusively from the diIr complex dopants in the emissive layer. Devices of complex 2 show especially impressive performance for a spin-coated active layer without full layer thickness optimization (Figures 12b–e). It is possible that the enhanced dipole moment and/or electron transport ability of complex 2, induced by the fluorine atoms on the cyclometalating ligands, are important factors in increasing the device efficiency.<sup>[41]</sup>

The most notable features are remarkably high maximum external quantum efficiency  $\eta_{\text{ext}}^{\max}$  ca. 20% and luminous efficiency up to  $\eta_{\text{L}}^{\max}$  26 cd/A. These values greatly exceed previous data for PhOLEDs of diiridium complexes bridged by a  $\mu_2$ -oxamidato-*N,N',O,O'* ligand ( $\eta_{\text{ext}}^{\max}$  3–3.5% and  $\eta_{\text{L}}^{\max}$  13 cd/A).<sup>[32]</sup> For comparison, to our knowledge, the highest reported efficiencies of PhOLEDs of any diiridium complexes are  $\eta_{\text{ext}}^{\max}$  25.1% ( $\lambda_{\max}^{\text{EL}}$  530 nm)<sup>[21]</sup> and  $\eta_{\text{ext}}^{\max}$  23.9% ( $\lambda_{\max}^{\text{EL}}$  602 nm).<sup>[17]</sup> A solution-processable emitting layer is desirable for low-cost, large-area devices and panels for lighting applications, with many advantages over ultra-high vacuum thermal evaporation processes.<sup>[42]</sup>



**Figure 11.** Simulated emission spectra from model geometries of *anti meso* isomers 1–3.

## Conclusions

This study has focussed on three new neutral  $C^N$  cyclo-metallated diiridium(III) complexes 1–3 bridged by a  $\mu_2$ -oxamidato- $N,N',O,O'$  ligand. The complexes are inseparable mixtures of diastereomers (*rac*,  $\Delta\Delta/\Lambda\Lambda$  and *meso*,  $\Delta\Lambda$ ) with bridges in *anti* and *syn* configurations but it was revealed that employing 2-fluorenylpyridine (fpy) as ligand leads unexpectedly to a dominant isomer of a diiridium  $\mu_2$ -oxamidato- $N,N',O,O'$  system in 1 and 3. The isomers in the fluorine-containing complex 2 from 5-fluoro-2-fluorenylpyridine (fpyF) could be determined here for the first time for a diiridium  $\mu_2$ -oxamidato- $N,N',O,O'$  system by using  $^{19}\text{F}$  NMR spectroscopy. The solution PL quantum yields,  $\Phi_{\text{PL}}$  57–82%, found for these three systems are unusually high for diiridium complexes. The phosphorescence originates from triplet mixed metal-ligand to ligand charge transfer states ( $^3\text{MLLCT}$ ). Calculations provide deeper analysis of the electronic and photophysical properties of the complexes, with close agreement between experimental and computed data. PhOLEDs have been fabricated using these complexes as the emissive dopants in a device architecture

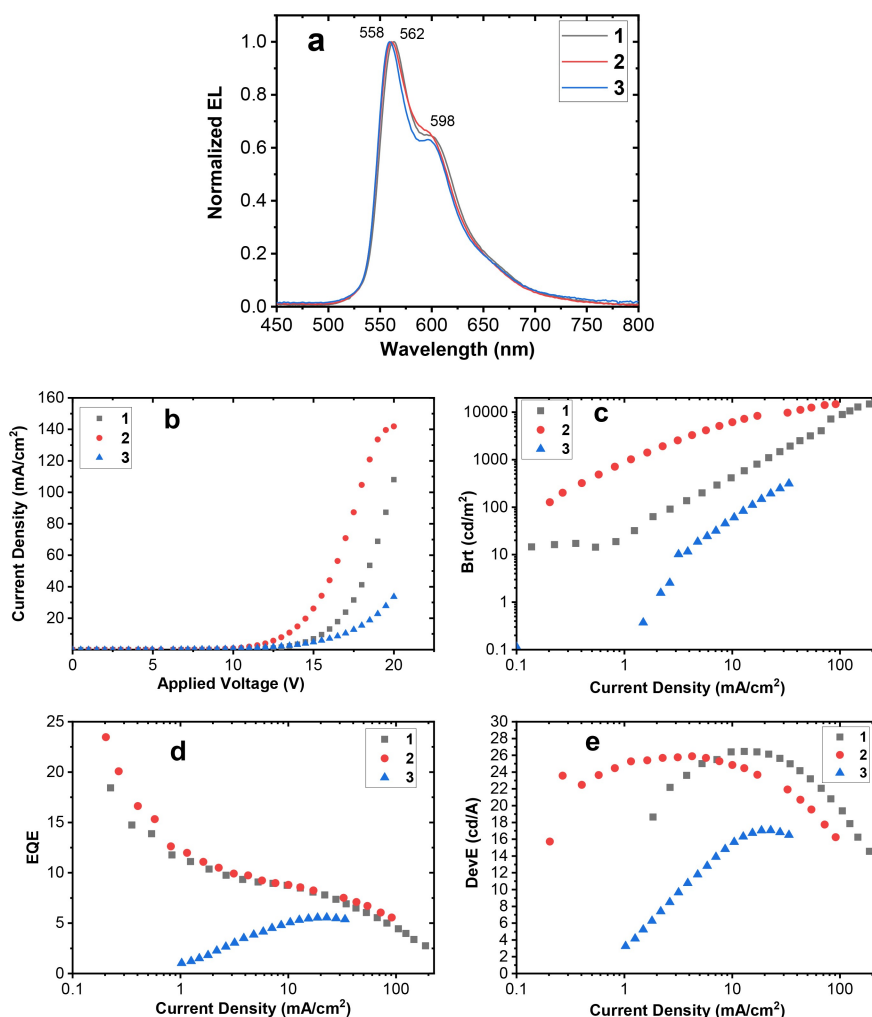


**Figure 12.** (a) Electroluminescence (EL) spectra of the devices with complexes 1, 2 or 3; (b) V–J characteristics, (c) J–Brt characteristics. (d) External quantum efficiency, and (e) Device current efficiency.

with a solution-processed active layer. The devices have bright greenish-yellow emission with  $\lambda_{\text{max}}^{\text{EL}}$  ca. 560 nm, with remarkably high maximum external quantum efficiency  $\eta_{\text{ext}}^{\text{max}}$  ca. 20% and luminous efficiency up to  $\eta_{\text{L}}^{\text{max}}$  26 cd/A. The molecular framework of these bridged structures is ideal for new chemical modifications that will tune the emission color and further enhance PHOLED performance.

## Experimental

### General

All commercial chemicals were used without further purification unless otherwise stated. Solvents were dried through an HPLC column on an Innovative Technology Inc. solvent purification system. Column chromatography was carried out using 40–60  $\mu\text{m}$  mesh silica. NMR spectra were recorded on a solution-state Bruker Neo-400 ( $^{19}\text{F}$ ), Varian V NMRS-600 ( $^1\text{H}$ ,  $^{13}\text{C}$ ) or Bruker Neo-700 ( $^1\text{H}$ ,  $^{13}\text{C}$ ) spectrometers (Figures 2 and S1–S18 for NMR spectra). Proton and carbon-13 NMR peaks for **1** and **3** were assigned with the aid of 2D  $^1\text{H}$ – $^1\text{H}$  COSY/NOESY and  $^1\text{H}$ – $^{13}\text{C}$  correlation (HSQC and HMBC) spectra (Figure 13). MALDI TOF MS data were obtained on a Bruker Autoflex II ToF/ToF mass spectrometer. Elemental analyses were performed on a CE-400 Elemental Analyzer. Thermal analysis was performed in a nitrogen atmosphere on a Perkin Elmer Pyris 1 instrument.

**Complex 1.** Solutions of sodium methoxide (7.55 mg, 0.14 mmol) in methanol (0.5 ml) and oxalamide (6.15 mg, 0.07 mmol) in methanol (3 ml) were mixed and stirred for 30 min at 20 °C. A solution of dichloro-dimer  $[\text{Ir}(\text{flpy})_2\text{Cl}_2]^{[37]}$  (113 mg, 0.054 mmol) in THF (10 ml) was added. The reaction mixture was stirred at 20 °C for 24 h. The solvent was removed and the crude product was dissolved in dichloromethane (DCM, 50 ml). Water (25 ml) was added and the DCM layer was separated and dried over magnesium sulfate then filtered. Methanol (25 ml) was added to the DCM layer. The solvent was partly removed using a rotavapor leaving the crude solid product and some solvent. The solid was filtered and purified by

column chromatography over silica gel, eluting with DCM (saturated with  $\text{K}_2\text{CO}_3$  and 2%  $\text{Et}_3\text{N}$ ) to give complex **1** (0.075 g, 66%) as an orange solid. MS(MALDI-ToF)  $m/z$  2113 ( $[\text{M}^+$ ,  $^{191}\text{Ir}$ ,  $^{193}\text{Ir}]$ , 100%). Anal. Calcd. for  $\text{C}_{122}\text{H}_{146}\text{Ir}_2\text{N}_6\text{O}_2$ : C, 69.35; H, 6.96; N, 3.98. Found: C, 69.11; H, 7.10; N, 3.75%. Crystals for X-ray analysis were grown from a solution of **1** in chlorobenzene/pentane.

$^1\text{H}$  NMR (700 MHz,  $\text{CDCl}_3$ );  $\delta$  8.90 (d, 2H, H6'), 8.81 (d, 2H, H6), 7.93 (d, 2H, H3'), 7.90 (d, 2H, H3), 7.79 (t, 2H, H4'), 7.72 (t, 2H, H4), 7.50 (s, 2H, H12), 7.48 (s, 2H, H12'), 7.31 (d, 2H, H18'), 7.27 (d, 2H, H18), 7.23 (t, 2H, H5'), 7.21 (d, 2H, H15'), 7.19 (d, 2H, H15), 7.14 (t, 4H, H16/17'), 7.13 (t, 4H, H16'/17), 7.11 (t, 2H, H5), 6.78 (s, 2H, H9), 6.60 (s, 2H, H9'), 6.09 (s, 2H, NH); 1.88, 1.84, 1.82, 1.79 (m, 16H, H20/20'/26/26'); 1.05, 1.02, 0.97, 0.95 (m, 16H, H24/24'/30/30'); 0.97, 0.95, 0.93, 0.91 (m, 16H, H22/22'/28/28'); 0.95, 0.95, 0.91, 0.90 (m, 16H, H23/23'/29/29'); 0.69, 0.68, 0.63, 0.61 (t, 24H, H25/25'/31/31'); 0.68, 0.61, 0.52, 0.49 (m, 16H, H21/21'/27/27').

$^{13}\text{C}\{^1\text{H}\}$  NMR (176 MHz,  $\text{CDCl}_3$ );  $\delta$  174.4 (C32/33), 169.7 (C2), 169.2 (C2'), 153.5 (C11/11'), 152.0 (C14), 152.0 (C14'), 150.0 (C6), 148.4 (C6'), 143.6 (C8), 143.5 (C8'), 143.3 (C10'), 143.2 (C10), 142.2 (C7'), 142.1 (C7), 141.3 (C13), 141.0 (C13'), 136.6 (C4'), 135.8 (C4), 126.8 (C16), 126.7 (C16'), 126.2 (C17), 126.2 (C17'), 124.1 (C9'), 123.5 (C9), 122.8 (C15), 122.8 (C15'), 120.7 (C5'), 120.7 (C5), 119.8 (C18), 119.7 (C18'), 118.8 (C12'), 118.7 (C3'), 118.5 (C12), 118.4 (C3); 54.2 (C19), 54.2 (C19'); 40.8, 40.6, 40.6, 40.5 (C20/20'/26/26'); 31.7, 31.6, 31.4, 31.3 (C23/23'/29/29'); 30.1, 29.9, 29.8, 29.7 (C22/22'/28/28'); 24.0, 23.9, 23.9, 23.8 (C21/21'/27/27'); 22.8, 22.7, 22.6, 22.6 (C24/24'/30/30'), 14.0, 14.0, 14.0, 14.0 (C25/25'/31/31').

**Complex 2.** The procedure was the same as for complex **1** now using  $[\text{Ir}(\text{flpyF})_2\text{Cl}_2]^{[37]}$  (350 mg, 0.161 mmol). Complex **2** (0.23 g, 65%) was obtained as an orange solid. MS(MALDI-ToF)  $m/z$  2185 ( $[\text{M}^+$ ,  $^{191}\text{Ir}$ ,  $^{193}\text{Ir}]$ , 100%). Anal. Calcd. for  $\text{C}_{122}\text{H}_{142}\text{F}_4\text{Ir}_2\text{N}_6\text{O}_2$ : C, 67.07; H, 6.55; N, 3.85. Found: C, 66.80; H, 6.80; N, 3.61%.

**Complex 3.** The procedure was the same as for complex **1** now using  $N,N'$ -di(*t*-butyl)phenyloxalamide $^{[43]}$  (83.26 mg, 0.23 mmol) and  $[\text{Ir}(\text{flpy})_2\text{Cl}_2]^{[38]}$  (350 mg, 0.168 mmol). Complex **3** (0.235 g, 59%) was obtained as an orange solid. MS(MALDI-ToF)  $m/z$  2377 ( $[\text{M}^+$ ,  $^{191}\text{Ir}$ ,  $^{193}\text{Ir}]$ , 100%). Anal. Calcd. for  $\text{C}_{142}\text{H}_{170}\text{Ir}_2\text{N}_6\text{O}_2$ : C, 71.74; H, 7.21; N,

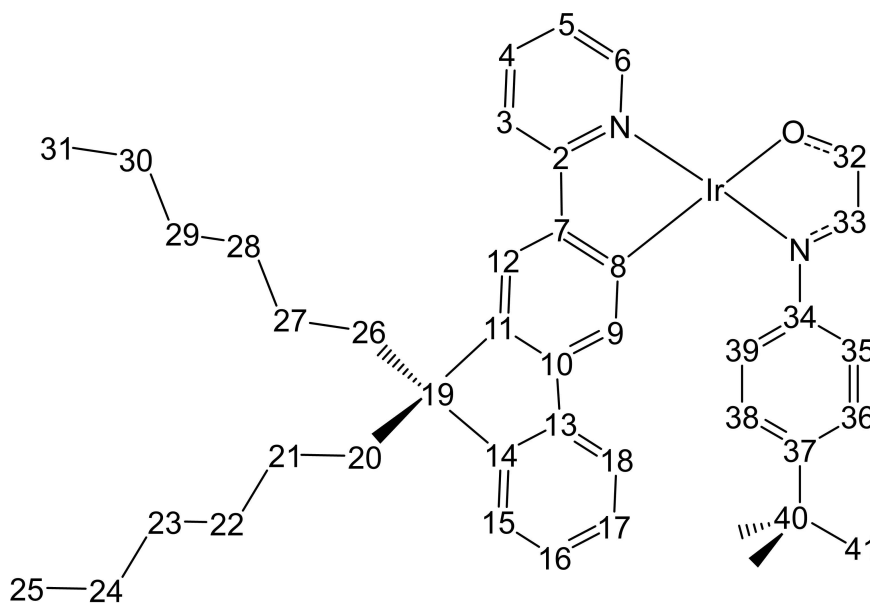


**Figure 13.** Atom numbering for  $^1\text{H}$  and  $^{13}\text{C}$  NMR peak assignments of **1** and **3**. The non-equivalent second flpy ligand atom numbering is denoted with ' (e.g. 2' for 2, 19' for 19).

3.54. Found: C, 71.55; H, 7.00; N, 3.72%. Crystals for X-ray analysis were grown from a solution of **3** in chlorobenzene/pentane.

$^1\text{H}$  NMR (700 MHz,  $\text{CDCl}_3$ );  $\delta$  9.07 (d, 2H, H6'), 8.81 (d, 2H, H6), 8.02 (d, 2H, H3'), 7.85 (t, 2H, H4'), 7.71 (d, 2H, H3), 7.67 (t, 2H, H4), 7.49 (s, 2H, H12'), 7.27 (s, 2H, H12), 7.26 (d, 2H, H18), 7.19 (t, 2H, H5'), 7.18 (d, 2H, H15'), 7.16 (d, 2H, H18'), 7.14 (d, 2H, H15), 7.10 (t, 2H, H5), 7.07 (t, 4H, H16/16'), 7.05 (t, 4H, H17/17'), 6.64 (s, 2H, H9), 6.56 (d, 4H, H35/39), 6.51 (d, 4H, H36/38), 6.40 (s, 2H, H9'), 1.82, 1.76, 1.75, 1.70 (m, 16H, H20/20'/26/26'); 1.14, 1.04, 0.87, 0.83 (m, 16H, H24/24'/30/30'); 1.10, 0.95, 0.77, 0.73 (m, 16H, H23/23'/29/29'); 1.08, 0.96, 0.80, 0.76 (m, 16H, H22/22'/28/28'); 0.94, 0.78, 0.46, 0.36 (m, 16H, H21/21'/27/27'); 0.91 (s, 18H, H41); 0.78, 0.70, 0.57, 0.53 (t, 24H, H25/25'/31/31').

$^{13}\text{C}\{^1\text{H}\}$  NMR (176 MHz,  $\text{CDCl}_3$ );  $\delta$  172.6 (C32/33), 170.3 (C2'), 168.8 (C2), 151.9 (C14), 151.8 (C14'), 150.2 (C6'/11'), 148.9 (C11), 148.5 (C6), 145.1 (C34), 143.7 (C8'), 143.4 (C10'), 142.9 (C37), 142.7 (C10), 142.2 (C7), 142.0 (C8, C7'), 141.4 (C13), 141.3 (C13'), 136.4 (C4'), 135.7 (C4), 126.4 (C16/16'), 126.1 (C17/17'), 125.0 (C35/39), 123.9 (C9'), 123.7 (C36/38), 123.4 (C9), 122.9 (C15'), 122.6 (C15), 120.9 (C5'), 120.0 (C5), 119.7 (C18), 119.6 (C18'), 118.5 (C3'), 118.3 (C12), 118.3 (C12'), 117.8 (C3); 54.1, 53.9 (C19/19'); 40.7, 40.3, 40.3, 40.1 (C20/20'/26/26'); 33.9 (C40); 31.4 (C41); 31.6, 31.5, 31.2, 31.1 (C23/23'/29/29'); 30.0, 30.0, 29.6, 29.5 (C22/22'/28/28'); 24.0, 23.9, 23.5, 23.4 (C21/21'/27/27'); 23.0, 22.8, 22.5, 22.4 (C24/24'/30/30'), 14.2, 14.1, 14.0, 14.0 (C25/25'/31/31').

### X-Ray Crystallography

Diffraction data for **1** were collected on a Rigaku Crystal Logic 4-circle  $\kappa$ -diffractometer with a Saturn 724+ CCD area detector at Station I19 of the Diamond Light Source synchrotron (undulator radiation, double-crystal Si monochromator,  $\lambda = 0.6889 \text{ \AA}$ ) and for **3** on a Bruker 3-circle APEX-II diffractometer with a PHOTON 100 CMOS area detector (Mo- $\text{K}\alpha$  radiation from an Incoatec  $\mu\text{S}$  microsource with focussing mirrors,  $\lambda = 0.71073 \text{ \AA}$ ), and corrected for absorption by empirical methods based on multiple scans and Laue equivalents (SADABS program).<sup>[44]</sup> The structures were solved by dual-space intrinsic phasing<sup>[45]</sup> (**1**) and Patterson (**3**) methods and refined by full-matrix least squares against  $F^2$  of all data using SHELXL program<sup>[46]</sup> on OLEX2-1.5 platform.<sup>[47]</sup> Structure **1** contains infinite channels parallel to the  $a$  axis, comprising 19% of the crystal volume and containing chaotically disordered solvent which could not be refined at atomic resolution, the residual electron density map showing a continuous, near-uniform 'chord' of electron density along the axis of the channel. Since the crystal was grown from PhCl/pentane solution and the channel has bottlenecks of  $< 3 \text{ \AA}$  diameter, which is too narrow for a chlorobenzene molecule, we assume that the random distribution of the solvent along the channel is only possible for pentane. The solvent was masked using the OLEX2 SMTBX program<sup>[48]</sup> which gave the total electron density of 116 e per unit cell, or ca. 3 molecules of pentane per formula unit of **1**.

Deposition numbers CCDC-2331774 (for **1**) and 2386358 (for **3**) contain the supplementary crystallographic data for this paper. These data are provided free of charge by the joint Cambridge Crystallographic Data Centre and Fachinformationszentrum Karlsruhe <http://www.ccdc.cam.ac.uk/structures> Access Structures service.

### Electrochemistry

Cyclic voltammograms were recorded at a scan rate of  $100 \text{ mVs}^{-1}$  at room temperature using an air-tight single-compartment three-electrode cell equipped with a Pt disk working electrode, Pt wire

counter electrode, and Pt wire pseudo-reference electrode. The cell was connected to a computer-controlled Autolab PG-STAT 30 potentiostat. The solutions contained the complex and  $n\text{-Bu}_4\text{NPF}_6$  (0.1 M) as the supporting electrolyte in dichloromethane (DCM). All potentials were determined with the decamethylferrocene/decamethylferrocenium couple as an internal reference in DCM at  $-0.55 \text{ V}$  for the usual reference standard of the ferrocene/ferrocenium couple ( $\text{FcH}/\text{FcH}^+$ ) in DCM at  $0.0 \text{ V}$ .

### Photophysical Measurements

UV-Vis and photoluminescence spectra were obtained with the Shimadzu UV-3600 spectrometer and Jobin Yvon Luminescence spectrometer (FluoroMax-3). Phosphorescence decay lifetime data were measured by time-resolved emission spectroscopy (TRES) using a pulsed Nd-yttrium aluminium garnet (Nd:YAG) laser ( $\lambda = 355 \text{ nm}$ ), repetition rate 1–10 Hz, FWHM 120 ps and maximum pulse energy of 7 mJ. The light emitted by the samples was dispersed through a spectrograph (TRIAX 180, Jobin Yvon-Spex) and the separated spectra were subsequently detected by a gated intensified charge coupled device (CCD) camera (4 pico, Stanford Computer Optics). The PL decay transients were obtained using exponentially increasing decay and integration times as previously described.<sup>[49]</sup> PLQYs were measured in degassed 2-MeTHF with three freeze-pump-thaw cycles, with 9,10-diphenylanthracene (DPA) in cyclohexane ( $\Phi_{\text{PL}} = 90\%$ )<sup>[50]</sup> as the standard.

### Computations

All calculations were employed with the Gaussian 16 package.<sup>[51]</sup> The 12 optimized geometries of the four isomers of **1–3** were carried out at the ground state  $S_0$  using B3LYP<sup>[52]</sup> with the pseudopotential (LANL2DZ)<sup>[53]</sup> for iridium and 3-21G\* basis set<sup>[54]</sup> for all other atoms. This model chemistry was selected on the basis of good agreements between experimental and computed data in related iridium complexes elsewhere.<sup>[18,19,32,34,44,55]</sup> Methyl groups were used instead of hexyl groups in these optimized geometries to reduce computational efforts. In addition, three excited state  $T_1$  geometries of **1–3** as *anti meso* isomers were also located. All geometries were found to be true minima with no imaginary frequencies found. Electronic structure calculations on the  $S_0$  geometries of the *anti meso* isomers at B3LYP/LANL2DZ:3-21G\* were used to obtain the calculated HOMO energies and the frontier molecular orbitals where % orbital contributions were obtained with the GaussSum package.<sup>[56]</sup>

Simulated emission spectra for related iridium complexes were recently shown to be in good agreement with experimental emission data.<sup>[57]</sup> Here, vibronic emission spectra were generated with adiabatic Hessian (AH) calculations from ground  $S_0$  and excited  $T_1$  state optimized geometries for the *anti meso* isomers of **1–3** at B3LYP/LANL2DZ:3-21G\*. The full width half height (FWHH) broadening value  $900 \text{ cm}^{-1}$  was applied and simulated spectra were produced visually with the GaussView package.<sup>[58]</sup>

The natural transition orbitals (NTOs) for the  $S_0$  geometries of **1–3** were obtained by time-dependent DFT (TD-DFT) calculations at B3LYP/LANL2DZ:3-21G\*. NTO figures and % orbital contributions for **1** were generated with the aid of Gabedit<sup>[59]</sup> and Multiwfn<sup>[60]</sup> packages, respectively. Best geometry fittings between the  $S_0$  and  $T_1$  geometries of the *anti meso* isomers based on root mean square (rms) errors (misfits in angstroms ( $\text{\AA}$ )) – the lower the value the better the fit) were determined with the OLEX2 package.<sup>[47]</sup>

## Device Fabrication and Measurements

The OLED devices were fabricated using precleaned indium tin oxide (ITO) coated glass substrate patterned to form four pixels of 4×4 mm in 24×24 mm samples, purchased from Kinetic. The ITO thickness was ca. 120 nm with a sheet resistance of 15 Ω square<sup>-1</sup>. The cleaned samples were exposed to UV-ozone for 10 min and purged with dry nitrogen. A hole injection layer of poly(3,4-ethylenedioxythiophene) polystyrene sulfonate (PEDOT:PSS) (4083) of thickness 40 nm was spin-coated at 5000 rpm for 1 min and then baked on a hotplate at 180 °C for 6 min to remove any remaining moisture. A chlorobenzene solution of poly(9-vinylcarbazole) (PVK) of molecular weight 90,000 (15 mg /ml) was both the host and a hole-transporting material. The PVK solution was doped with 40% w/w of (1,3-phenylene)bis[5-(4-*tert*-butylphenyl)-1,3,4-oxadiazole] (OXD-7) as an electron-transporting material for balancing charge carrier transport. Complexes 1–3 readily dissolved in chlorobenzene without any aggregated particulates. A mixture of PVK (15 mg) OXD-7 (40 wt%) and the complex (2 wt%) was spin-coated at 3000 rpm for 1 min on the top of the PEDOT:PSS layer and baked for 10 min at 110 °C. Each sample was shadow-masked to produce four identical devices of area 4×4 mm; the samples were then introduced into a nitrogen glove box, where 2,2',2''-(1,3,5-benzenetriyl)tris-[1-phenyl-1*H*-benzimidazole] (TPBi) (30 nm) was evaporated as a hole-blocking layer at a rate of ~1 Å/s under vacuum at a pressure of ca. 1×10<sup>-6</sup> torr, followed by 2,9-dimethyl-4,7-diphenyl-1,10-phenanthroline [bathocuproine (BCP)] (8 nm) as an electron-injection layer followed by LiF (0.7 nm) and Al (100 nm) cathodes at a rate of 0.2 and 1 Å s<sup>-1</sup>, respectively, under the same vacuum conditions. The devices were then encapsulated with DELO UV curable epoxy (Katiobond) and a 12×12 mm glass cover slide. The final device structure was ITO/PEDOT:PSS (40 nm)/[PVK:OXD-7 (40 wt%):Ir complex (1 or 2 or 3)(2 wt%)]/TPBi (30 nm)/BCP(8 nm)/LiF (0.7 nm)/Al (100 nm). The current–voltage (*I*–*V*) characteristics and the emission intensities were measured in a calibrated Labsphere LMS-100 integrating sphere and the data acquisition was controlled using a home-written NI LabView program that controlled an Agilent Technologies 6632B power supply. The EL spectra were measured using an Ocean Optics USB 4000 CCD spectrometer supplied with a 400 μm UV–Vis fibre optic cable.

## Acknowledgments

Funding for this research was provided by Deanship of Scientific Research at Prince Sattam Bin Abdulaziz University (grant No. 19803/01/2022 to A. M'hamed). The Diamond Light Source (RAL) is thanked for the award of instrument time on Station I19 (MT 11145) and the instrument scientists for their kind support.

## Conflict of Interests

The authors declare no conflict of interest.

## Data Availability Statement

The data that support the findings of this study are available in the supplementary material of this article.

**Keywords:** Iridium complex · Bimetallic · Luminescence · X-ray crystallography · Density functional theory · Phosphorescent organic light emitting diode

- [1] H. Yersin, *Top. Curr. Chem.* **2004**, *241*, 1–26.
- [2] a) B. Doistau, J. R. Jiménez, C. Piquet, *Front. Chem.* **2020**, *8*, 555; b) Z.-G. Niu, H.-B. Han, M. Li, Z. Zhao, G.-Y. Chen, Y.-X. Zheng, G.-N. Li, J.-L. Zuo, *Organometallics* **2018**, *37*, 3154–3164; c) P. N. Lai, S. Yoon, T. S. Teets, *Chem. Commun.* **2020**, *56*, 8754–8757; d) A. Bonfiglio, M. Mauro, *Eur. J. Inorg. Chem.* **2020**, *36*, 3427–2442; e) J. Soellner, T. Strassner, *Eur. J. Inorg. Chem.* **2021**, 601–604; f) G. Millan, M. Nieddu, I. P. Lopez, C. Ezquerro, J. R. Berenguer, I. M. Larrayoz, J. G. Pichel, E. Lalinde, *Dalton Trans.* **2023**, *52*, 6360–6374; g) C. E. Elgar, H. Y. Otaif, J. M. Beames, P. N. Horton, S. J. Coles, A. J. Hallett, S. P. O'Kell, S. J. A. Pope, *Eur. J. Inorg. Chem.* **2023**, *26*, e202300102; h) K. S. Bejymohandas, B. Ventura, A. Baschierri, A. Mazzanti, E. Bandini, F. Monti, *Eur. J. Inorg. Chem.* **2024**, doi.org/10.1002/ejic.202400224.
- [3] M. A. Baldo, D. F. O'Brien, Y. You, A. Shoustikov, S. Sibley, M. E. Thompson, S. R. Forrest, *Nature* **1998**, *395*, 151–154
- [4] T.-Y. Li, J. Wu, Z.-G. Wu, Y.-X. Zheng, J.-L. Zuo, Y. Pan, *Coord. Chem. Rev.* **2018**, *374*, 55–92
- [5] H.-T. Miao, G.-F. Li, G.-G. Shan, X.-L. Wang, Z.-M. Su, *Coord. Chem. Rev.* **2020**, *413*, 213283.
- [6] S. Ladouceur, E. Zysman-Colman, *Eur. J. Inorg. Chem.* **2013**, 2985–3007.
- [7] R. D. Costa, E. Ortí, H. J. Bolink, F. Monti, G. Accorsi, N. Armaroli, *Angew. Chem. Int. Ed.* **2012**, *51*, 8178–8211.
- [8] B. H. Jhun, D. Song, S. Y. Park, Y. You, *Top. Curr. Chem.* **2022**, *380*, 35.
- [9] C.-P. Tan, Y.-M. Zhong, L.-N. Ji, Z.-W. Mao, *Chem. Sci.* **2021**, *12*, 2357–2367.
- [10] D. N. Tritton, F.-K. Tang, G. B. Bodedla, F.-W. Lee, C.-S. Kwan, K. C.-F. Leung, X. Zhu, W.-Y. Wong, *Coord. Chem. Rev.* **2022**, *459*, 214390.
- [11] Z.-Qiu, Li, Z.-L. Gong, T. Liang, S. Bernhard, Y.-W. Zhong, J. Yao, *Sci. China Chem.* **2023**, *66*, 2892–2902.
- [12] L. F. Gildea, J. A. G. Williams, Woodhead Publishing **2013** Iridium and platinum complexes for OLEDs, in *Organic Light-Emitting Diodes: Materials, Devices and Applications*, A. Buckley (Editor).
- [13] G. Li, D. Zhu, X. Wang, Z. Su, M. R. Bryce, *Chem. Soc. Rev.* **2020**, *49*, 765–838.
- [14] M. Z. Shafikov, R. Daniels, V. N. Kozhevnikov, *J. Phys. Chem. Lett.* **2019**, *10*, 7015–7024.
- [15] M. Z. Shafikov, R. Martinscroft, C. Hodgson, A. Hayer, A. Auch, V. N. Kozhevnikov, *Inorg. Chem.* **2021**, *60*, 1780–1789.
- [16] X. Yang, X. Xu, J. S. Dang, G. Zhou, C. L. Ho, W. Y. Wong, *Inorg. Chem.* **2016**, *55*, 1720–1727.
- [17] X. Yang, X. Chen, J. Dang, Y. Sun, Z. Feng, Z. Tian, G. Zhou, Z. Wu, *Chem. Eng. J.* **2020**, *391*, 123505.
- [18] Y. Zheng, A. S. Batsanov, M. A. Fox, H. A. Al-Attar, K. Abdullah, V. Jankus, M. R. Bryce, A. P. Monkman, *Angew. Chem. Int. Ed.* **2014**, *53*, 11616–11619.
- [19] D. G. Congrave, Y.-T. Hsu, A. S. Batsanov, A. Beeby, M. R. Bryce, *Dalton Trans.* **2018**, *47*, 2086–2098.
- [20] J. L. Liao, P. Rajakannu, P. Gnanasekaran, S. R. Tsai, C. H. Lin, S. H. Liu, C. H. Chang, G. H. Lee, P. T. Chou, Z. N. Chen, Y. Chi, *Adv. Opt. Mater.* **2018**, *6*, 1800083.
- [21] Y. Yuan, P. Gnanasekaran, Yu-W. Chen, G.-H. Lee, S.-F. Ni, C.-S. Lee, Y. Chi, *Inorg. Chem.* **2020**, *59*, 523–532.
- [22] X.-H. Yang, M. Li, H. Peng, Q. Zhang, S.-X. Wu, W.-Q. Xiao, X.-L. Chen, Z.-G. Niu, G.-Y. Chen, G.-N. Li, *Eur. J. Inorg. Chem.* **2019**, 847–855.
- [23] G. Li, X. Ren, G. Shan, W. Che, D. Zhu, L. Yan, Z. Su, M. R. Bryce, *Chem. Commun.* **2015**, *51*, 13036–13039.
- [24] Y. Jiang, G. Li, W. Che, Y. Liu, B. Xu, G. Shan, D. Zhu, Z. Su, M. R. Bryce, *Chem. Commun.* **2017**, *53*, 3022–3025.
- [25] Y. He, G. Fu, W. Li, B. Wang, T. Miao, M. Tan, W. Feng, X. Lü, *J. Luminescence* **2020**, *218*, 116847.
- [26] M.-G. La-Placa, A. M. Igual-Muñoz, J. Romero, R. E. Daniels, V. N. Kozhevnikov, M. Sessolo, H. J. Bolink, *ECS J. Solid State Sci. Technol.* **2019**, *8*, R84–R87.
- [27] K. Sasaki, K. Okamoto, K. Ohe, *Eur. J. Inorg. Chem.* **2020**, 1894–1901.
- [28] J. Fernández-Cestau, N. Giménez, E. Lalinde, P. Montaña, M. T. Moreno, S. Sánchez, *Organometallics* **2015**, *34*, 1766–1778.
- [29] C. G. L. Nongpiur, D. F. Diengdoh, N. Nagar, K. M. Poluri, P. M. Gannon, W. Kaminsky, M. R. Kollipara, *Polyhedron* **2022**, *227*, 116096.

- [30] J.-P. Sauvage, J.-C. Collin, J.-C. Chambron, S. Guillerez, C. Coudret, V. Balzani, F. Barigelletti, L. De Cola, L. Flamigni, *Chem. Rev.* **1994**, *94*, 993–1019.
- [31] M. Graf, R. Czerwieńiec, K. Sünkel, *Z. Anorg. Allg. Chem.* **2013**, *639*, 1090–1094.
- [32] A. M'hamed, M. A. Fox, A. S. Batsanov, H. A. Al-Attar, A. P. Monkman, M. R. Bryce, *J. Mater. Chem. C* **2017**, *5*, 6777–6789.
- [33] A. M'hamed, A. S. Batsanov, *Acta Cryst.* **2020**, *E76*, 392–399.
- [34] A. M'hamed, A. S. Batsanov, M. A. Fox, J. A. Aguilar, M. R. Bryce, *Eur. J. Inorg. Chem.* **2023**, e202300423.
- [35] J. C. Ostrowski, M. R. Robinson, A. J. Heeger, G. C. Bazan, *Chem. Commun.* **2002**, *7*, 784–785.
- [36] M. Tavasli, S. Bettington, M. R. Bryce, H. A. Al-Attar, F. B. Dias, S. King, A. P. Monkman, *J. Mater. Chem. C* **2005**, *15*, 4963–4970.
- [37] A. M'hamed, A. S. Batsanov, M. A. Fox, M. R. Bryce, K. Abdullah, H. A. Al-Attar, M. R. Bryce, *J. Mater. Chem. C* **2012**, *22*, 13529–13540.
- [38] I. Haiduc, *J. Coord. Chem.* **2020**, *73*, 1619–1700.
- [39] S. Lamansky, P. Djurovich, D. Murphy, F. Abdel-Razzaq, R. Kwong, I. Tsyba, M. Bortz, B. Mui, R. Bau, M. E. Thompson, *Inorg. Chem.* **2001**, *40*, 1704–1711.
- [40] P. J. Hay, *J. Phys. Chem. A* **2002**, *106*, 1634–1641.
- [41] H. A. Al-Attar, G. C. Griffiths, T. N. Moore, M. Tavasli, M. A. Fox, M. R. Bryce, A. P. Monkman, *Adv. Funct. Mater.* **2011**, *21*, 2376–2382.
- [42] J. Y. Woo, M.-H. Park, S.-H. Jeong, Y.-H. Kim, B. Kim, T.-W. Lee, T.-H. Han, *Adv. Mater.* **2023**, *35*, 2207454.
- [43] I. Welterlich, O. Charov, B. Tieke, *Macromolecules* **2012**, *45*, 4511–4519.
- [44] L. Krause, R. Herbst-Irmer, G. M. Sheldrick, D. Stalke, *J. Appl. Crystallogr.* **2015**, *48*, 3–10.
- [45] G. M. Sheldrick, *Acta Crystallogr.* **2015**, *A71*, 3–8.
- [46] G. M. Sheldrick, *Acta Crystallogr.* **2015**, *C71*, 3–8.
- [47] O. V. Dolomanov, L. J. Bourhis, R. J. Gildea, J. A. K. Howard, H. Puschmann, *J. Appl. Crystallogr.* **2009**, *42*, 339–341.
- [48] B. Rees, L. Jenner, M. Yusupov, *Acta Crystallogr.* **2005**, *D61*, 1299–1301.
- [49] C. Rothe, A. P. Monkman, *Phys. Rev. B* **2003**, *68*, 075208.
- [50] S. Hamai, F. Hirayama, *J. Phys. Chem.* **1983**, *87*, 83–89.
- [51] M. J. Frisch, G. W. Trucks, H. B. Schlegel, G. E. Scuseria, M. A. Robb, J. R. Cheeseman, G. Scalmani, V. Barone, G. A. Petersson, H. Nakatsuji, X. Li, M. Caricato, A. V. Marenich, J. Bloino, B. G. Janesko, R. Gomperts, B. Mennucci, H. P. Hratchian, J. V. Ortiz, A. F. Izmaylov, J. L. Sonnenberg, D. Williams-Young, F. Ding, F. Lipparini, F. Egidi, J. Goings, B. Peng, A. Petrone, T. Henderson, D. Ranasinghe, V. G. Zakrzewski, J. Gao, N. Rega, G. Zheng, W. Liang, M. Hada, M. Ehara, K. Toyota, R. Fukuda, J. Hasegawa, M. Ishida, T. Nakajima, Y. Honda, O. Kitao, H. Nakai, T. Vreven, K. Throssell, J. A. Montgomery, Jr., J. E. Peralta, F. Ogliaro, M. J. Bearpark, J. J. Heyd, E. N. Brothers, K. N. Kudin, V. N. Staroverov, T. A. Keith, R. Kobayashi, J. Normand, K. Raghavachari, A. P. Rendell, J. C. Burant, S. S. Iyengar, J. Tomasi, M. Cossi, J. M. Millam, M. Klene, C. Adamo, R. Cammi, J. W. Ochterski, R. L. Martin, K. Morokuma, O. Farkas, J. B. Foresman, D. J. Fox, Gaussian 16, Revision B.01, Gaussian, Inc., Wallingford CT, **2016**.
- [52] a) A. D. Becke, *J. Chem. Phys.* **1993**, *98*, 5648–5652; b) C. Lee, W. Yang, R. G. Parr, *Phys. Rev. B* **1988**, *37*, 785–789.
- [53] a) T. H. Dunning Jr., P. J. Hay, in *Modern Theoretical Chemistry*, (Ed: H. F. Schaefer III) Vol. 3, Plenum, New York, **1976**; b) P. J. Hay, W. R. Wadt, *J. Chem. Phys.* **1985**, *82*, 270–283; c) W. R. Wadt, P. J. Hay, *J. Chem. Phys.* **1985**, *82*, 284–298; d) P. J. Hay, W. R. Wadt, *J. Chem. Phys.* **1985**, *82*, 299–310.
- [54] a) G. A. Petersson, M. A. Al-Laham, *J. Chem. Phys.* **1991**, *94*, 6081–6090; b) G. A. Petersson, A. Bennett, T. G. Tensfeldt, M. A. Al-Laham, W. A. Shirley, J. Mantzaris, *J. Chem. Phys.* **1988**, *89*, 2193–2218.
- [55] a) H. A. Al-Attar, G. C. Griffiths, T. N. Moore, M. Tavasli, M. A. Fox, M. R. Bryce, A. P. Monkman, *Adv. Funct. Mater.* **2011**, *21*, 2376–2382; b) M. Tavasli, T. N. Moore, Y. Zheng, M. R. Bryce, M. A. Fox, G. C. Griffiths, V. Jankus, H. A. Al-Attar, A. P. Monkman, *J. Mater. Chem.* **2012**, *22*, 6419–6428; c) H. Benjamin, Y. Zheng, A. S. Batsanov, M. A. Fox, H. A. Al-Attar, A. P. Monkman, M. R. Bryce, *Inorg. Chem.* **2016**, *55*, 8612–8627; d) H. Benjamin, M. A. Fox, A. S. Batsanov, H. A. Al-Attar, C. Li, Z. Ren, A. P. Monkman, M. R. Bryce, *Dalton Trans.* **2017**, *46*, 10996–11007; e) H. Benjamin, Y. Zheng, V. N. Kozhevnikov, J. S. Siddle, L. J. O'Driscoll, M. A. Fox, A. S. Batsanov, G. C. Griffiths, F. B. Dias, A. P. Monkman, M. R. Bryce, *Dalton Trans.* **2020**, *49*, 2190–2208; f) R. M. Edkins, Y.-T. Hsu, M. A. Fox, D. Yufit, A. Beeby, R. J. Davidson, *Organometallics* **2022**, *41*, 2487–2493; g) R. Davidson, Y.-T. Hsu, M. A. Fox, J. A. Aguilar, D. Yufit, A. Beeby, *Inorg. Chem.* **2023**, *62*, 2793–2805; h) Y.-T. Hsu, C. Bhagani, J. A. Aguilar, M. A. Fox, D. Yufit, R. Davidson, A. Beeby, *Dalton Trans.* **2024**, *53*, 17518–17524.
- [56] N. M. O'Boyle, A. L. Tenderholt, K. M. Langner, *J. Comput. Chem.* **2008**, *29*, 839–845.
- [57] C. F. R. Mackenzie, S.-Y. Kwak, S. Kim, E. Zysman-Colman, *Dalton Trans.* **2023**, *52*, 4112–4121.
- [58] R. Dennington, T. Keith, J. Millam, Semichem Inc., Shawnee Mission, KS, 2019, GaussView, Version 6.
- [59] A. R. Allouche, *J. Comput. Chem.* **2011**, *32*, 174–182.
- [60] T. Lu, F. Chen, *J. Comput. Chem.* **2012**, *33*, 580–592.

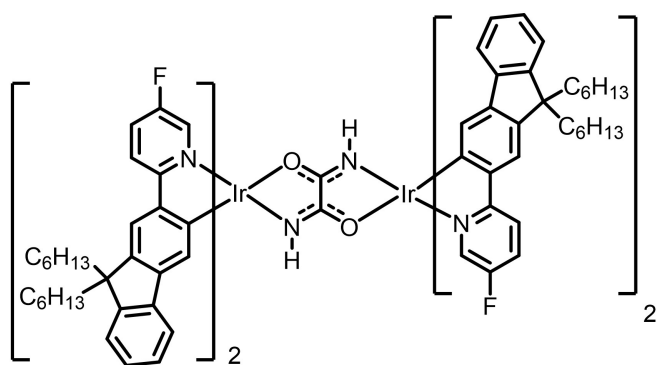
Manuscript received: November 8, 2024

Revised manuscript received: December 11, 2024

Accepted manuscript online: December 16, 2024

Version of record online: ■■, ■■

## RESEARCH ARTICLE



PhOLED:  $\text{EQE}_{\text{max}}^{\text{EL}}$  20%;  $\lambda_{\text{max}}^{\text{EL}}$  560 nm

Diiridium complexes bridged by  $\mu_2^-$ -oxamidato ligands give highly efficient phosphorescent organic light

emitting diodes with greenish-yellow emission.

Dr. A. M'hamedi, Dr. M. A. Fox, Dr. A. S. Batsanov, Dr. H. A. Al-Attar, Prof. M. R. Bryce\*

1 – 14

**Diiridium(III) Complexes with Fluorenylpyridyl Cyclometalating and  $\mu_2^-$ -Oxamidato Bridging Ligands and their High Efficiency Phosphorescent Solution-Processed OLEDs**

